

# Inversion of vortex flow around active microalgae under strong confinement

Debasmita Mondal,<sup>1</sup> Ameya G. Prabhune,<sup>1,2</sup> Sriram Ramaswamy,<sup>3</sup> and Prerna Sharma<sup>1,\*</sup>

<sup>1</sup>*Department of Physics, Indian Institute of Science,  
Bangalore, Karnataka 560012, India*

<sup>2</sup>*Department of Physics, University of Colorado Boulder, Boulder, Colorado 80309, USA.*

<sup>3</sup>*Centre for Condensed Matter Theory,  
Department of Physics, Indian Institute of Science,  
Bangalore, Karnataka 560012, India*

## Abstract

Active microorganisms swim in a viscous fluid and imprint characteristic signatures of their propulsion mechanisms in the generated flow fields. Confinement of these swimmers often arises in both natural and technological contexts. A well-developed theoretical understanding of such confined flows is available but does not include the effect of confinement on the motility itself. Here, we show that closely confining the microalga *Chlamydomonas* between two parallel plates does not merely inhibit motility but gives rise to flow features such as inversion of vortex flows quite distinct from expectations based on conventional theoretical analysis. We show that a conceptually simple quasi-2D steady Brinkman approximation to the Stokes equation yields a more satisfactory description of the observed flows than the usual method of images. Our results imply that confined active flows show a richer phenomenology than previously predicted and provide a methodology to analyse collective flows of confined swimmers.

---

\* [prerna@iisc.ac.in](mailto:prerna@iisc.ac.in)

## INTRODUCTION

Active microswimmers moving through viscous fluids are ubiquitous in the living world as well as in emerging nano- and microtechnologies [1]. Apart from microorganisms such as bacteria, sperm and algae, many artificial realizations are now available with applications in diagnostics, microfluidics, transport and drug delivery [2–5]. They achieve self-propulsion by converting stored or ambient free energy into systematic mechanical motion [6] and exhibit a rich and complex range of nonequilibrium phases and topological defect dynamics [7–11]. Microswimmers operate at low Reynolds number [12] where viscous fluid drag dominates over inertia in all functional and mechanical responses such as embryonic symmetry breaking, enhanced transport in suspensions, prey-predator dynamics, mechanosensing, flagellar mechanics, rheology and collective behaviour [13–16].

Confinement of microswimmers is prevalent in their natural world, for example spermatozoa swim through the narrow reproductive tract, bacteria and algae form dense biofilms [1, 17–22]. The introduction of boundaries alters both their motility and flow fields through steric and hydrodynamic interactions [13, 23] with important emergent consequences [24–26]. Understanding these effects has technological implications for realizing autonomous motion through microchannels for biomedical applications [5, 27, 28]. In this study, we identify the effect of strong confinement on the motility and hydrodynamics of a model microswimmer, *Chlamydomonas reinhardtii* (CR) in a quasi-2D chamber of height  $H$  comparable to the CR’s body diameter  $D \sim 10 \mu\text{m}$ . The unicellular, biflagellated alga CR, used extensively in studying active and biological fluid dynamics [29, 30], is widely appreciated as a model organism for understanding cellular processes in biology such as phototaxis and ciliary beating [31] and more recently as a sustainable biofuel source [32, 33]. CR is a classic example of an active puller in 3D, drawing fluid in along the propulsion axis and ejecting it in the perpendicular plane [13]. To compare cellular motility and flow under strong confinement to the weakly confined or bulk case, we also study CR in  $H = 30 \mu\text{m}$  (denoted ‘H30’ cells).

Here, we show that both the motility and flow field of CR are dramatically altered under strong confinement,  $H = 10 \mu\text{m}$ . First, observations of their flagellar waveform distinguish two subpopulations of cells depending on body diameter, (a) Synchronously beating cells typical of a CR (‘H10 Synchronous’), (b) Wobblers with asynchronous/paddler beat (‘H10 Wobbler’). Second, the cellular speed decreases significantly and the trajectory tortuosity increases with increasing confinement as we go from H30 to H10 cells. Third, the experi-

mental flow field of H10 Synchronous cells has opposite flow vorticity, not only to that in the bulk, but also to those predicted from the source dipole theory of confined swimmers [34, 35]. We replace the complicated and expensive method of recursive images [34, 36] for the Stokes equation by a simplified theoretical treatment for the flow fields, based on a quasi-2D Brinkman approximation [37], which we show is adequate for understanding the observed results. Solving this equation, we show that the vortex flow inversion arises due to two Gaussian force densities rather than the conventional three overall neutral point forces for CR [38]. Our experimental results establish that confinement not only alters the hydrodynamics but also modifies the swimmer motility which in turn impacts the fluid flows. Most theoretical studies do not address the latter effect, as it is difficult to predict the exact change in the swimmer propulsion and motility due to confinement. Furthermore, our robust and efficient description using point forces in a quasi-2D Brinkman equation is simple enough to implement and analyse confined flows in a wide range of biological and synthetic active systems.

## RESULTS

### Experimental System

Wild-type CR cells (strain CC 1690) propel themselves through a fluid medium by the characteristic breaststroke motion of two  $\sim 11$   $\mu\text{m}$  long anterior flagella with beat frequency  $\nu_b \sim 50 - 60$  Hz. The cells are synchronously grown in 12:12 hour light:dark cycle in Tris-Acetate-Phosphate (TAP+P) medium [39]. Cell suspension is collected in the logarithmic growth phase within the first 2-3 hours of light cycle and re-suspended in fresh TAP+P medium. After 30 minutes, they are introduced in rectangular quasi-2D chambers (area,  $18 \text{ mm} \times 6 \text{ mm}$ ) made up of a glass slide and coverslip sandwich with double tape of thickness  $H = 10/30$   $\mu\text{m}$  as spacer (Nitto Denko Corporation). Passive 200 nm sulfate latex microspheres are added as tracers to the cell suspension for measuring the fluid flow using particle tracking velocimetry (PTV). We use high speed video microscopy at  $\sim 500$  frames/second to capture flagellar waveform, cellular and tracer motion in the  $x-y$  plane at a distance  $H/2$  from the solid walls, with a 40X phase objective in red light illumination ( $> 610$  nm) to prevent phototaxis [40] and flagellar adhesion [41] of CR. The detailed experimental procedure is described in the Methods section.

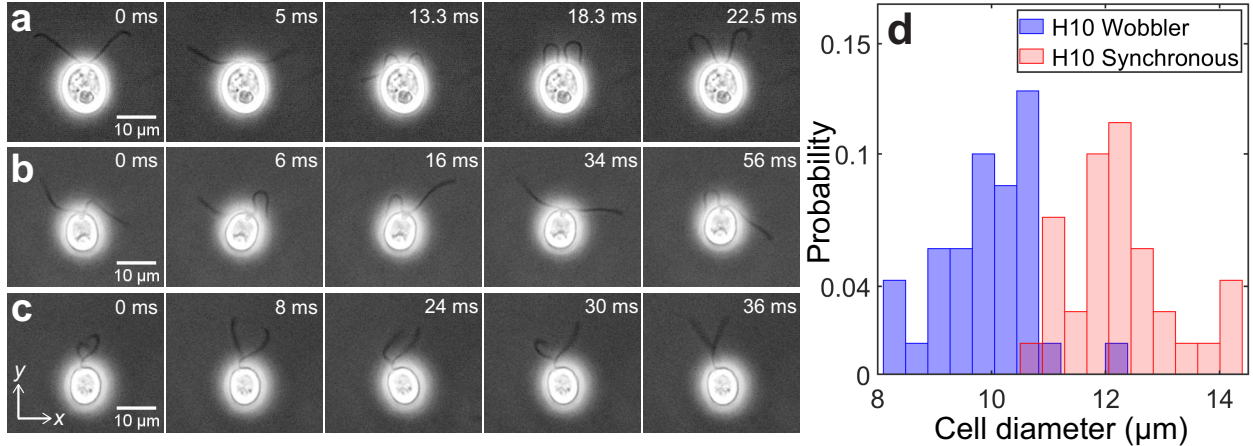


FIG. 1. **Flagellar waveform of cells in strong confinement.** Time lapse images of *Chlamydomonas* cells swimming in a quasi-2D chamber of height  $H = 10 \mu\text{m}$ , bounded by solid walls. (a) Synchronously beating flagella of a cell with diameter  $D \sim 13.2 \mu\text{m}$ . Flagellar beat frequency,  $\nu_b \sim 39 \text{ Hz}$ ; (b) Asynchronously beating flagella of a cell with  $D \sim 9.9 \mu\text{m}$ ; (c) Paddler type flagellar beat of a cell whose  $D \sim 9.7 \mu\text{m}$ . The cell bodies in (b) and (c) wobble due to their irregular flagellar beat pattern and are called ‘Wobblers’. (d) Histogram of cell body diameter in strong confinement,  $H = 10 \mu\text{m}$  (Number of cells,  $n = 70$ ). Synchronously beating cells ( $n = 34$ ) typically have larger diameter than Wobblers ( $n = 36$ ).

### Flagellar waveform and cell motility under strong confinement

CR cells confined to swim in  $H = 10 \mu\text{m}$  show three kinds of flagellar waveform as follows: (a) synchronous breaststroke and planar beating of flagella interrupted by intermittent phase slips (Fig. 1a, Supplementary Movie S1); (b) asynchronous and planar flagellar beat over large time periods (Fig. 1b, Supplementary Movie S2); both (a) and (b) are typically observed for CR in bulk [42], and (c) a distinctive paddling flagellar beat (Fig. 1c, Supplementary Movie S2) which is not observed in bulk CR swimmers. This beat is totally different from the conventional breaststroke motion as the pair of flagella paddle irregularly anterior to the cell, often wind up, with their beat plane mostly oriented perpendicular to the  $x - y$  plane (Fig. 1c and Supplementary Movie S2). The cell body wobbles for both asynchronous and paddler beat of cells (Fig. 1b & c) and often the flagellar waveform in a single CR switches between these two kinds (Supplementary Movie S2). Hence, we collectively call them ‘Wobblers’ [43, 44].

We can correlate the Synchronous and Wobbler nature of cells to their body diameter

(Fig. 1d). The mean diameter of Synchronous cells ( $D = 12.28 \pm 0.94 \mu\text{m}$ ,  $n = 34$ ) is higher than that of Wobblers ( $D = 9.92 \pm 0.85 \mu\text{m}$ ,  $n = 36$ ). Hence, the former's cell body is squished and very strongly confined in  $H = 10 \mu\text{m}$  than the latter. This leads to planar swimming of Synchronous cells, whereas Wobblers try to spin about their body axis and trace out a helical trajectory. This is the natural motility mechanism of the ellipsoidal cell body of CR in bulk to scan the incident light from all directions through its eyespot for efficient photosynthesis [45, 46]. Thus, the Wobblers that are not restrained enough tend to sweep a helical trajectory but end up compromising their flagellar beat into asynchrony and/or paddling due to the solid boundaries.

The trajectory of CR cells in  $H = 30 \mu\text{m}$  is similar to that of bulk and has the signature of back and forth cellular motion due to recovery and power strokes of flagella (Fig. 2a,d). As confinement increases, the drag on the cells due to solid walls increases and they trace out smaller distances with increasing twists and turns in the trajectory (Fig. 2a-f). These phenomena can be quantitatively characterized by cell speed and trajectory tortuosity (see Methods for definition and details) as a function of  $D_{avg}/H$ , which denotes the effect of confinement on cells (Fig. 2g). Cellular speed decreases and tortuosity of trajectories increases with increasing  $D_{avg}/H$  as we go from H30  $\rightarrow$  H10 Wobbler  $\rightarrow$  H10 Synchronous

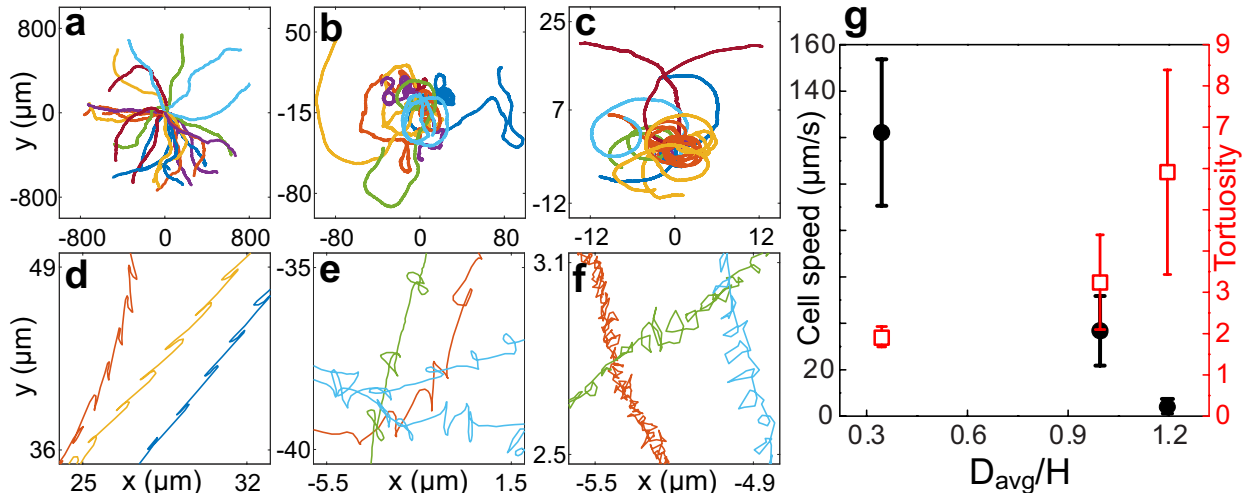


FIG. 2. **Cell motility in weak and strong confinement.** Trajectories of *Chlamydomonas* cells in (a)  $H = 30 \mu\text{m}$ , (b)  $H = 10 \mu\text{m}$ , Wobblers; (c)  $H = 10 \mu\text{m}$ , Synchronous. All of these trajectories lasted for 8.2 s and their initial positions are shifted to origin. (d), (e) and (f) are the zoomed in trajectories of (a), (b) and (c), respectively. (g) Cell speed (circles) and tortuosity of trajectories (squares) as a function of average cell diameter/chamber height ( $D_{avg}/H$ ).

cells. Notably, the cell speed  $u$  decreases by 96% from H30 ( $\langle u \rangle = 122.14 \pm 31.59 \mu\text{m/s}$ ,  $n = 52$ ) to H10 Synchronous ( $\langle u \rangle = 4.07 \pm 2.88 \mu\text{m/s}$ ,  $n = 23$ ).

### Experimental flow fields

We measure the beat averaged flow fields of H30 and H10 Synchronous CR cells to systematically understand the effect of strong confinement on the swimmer's flow field. We consider the flow field for H30 cells only when their flagellar beat is in the  $x - y$  plane and

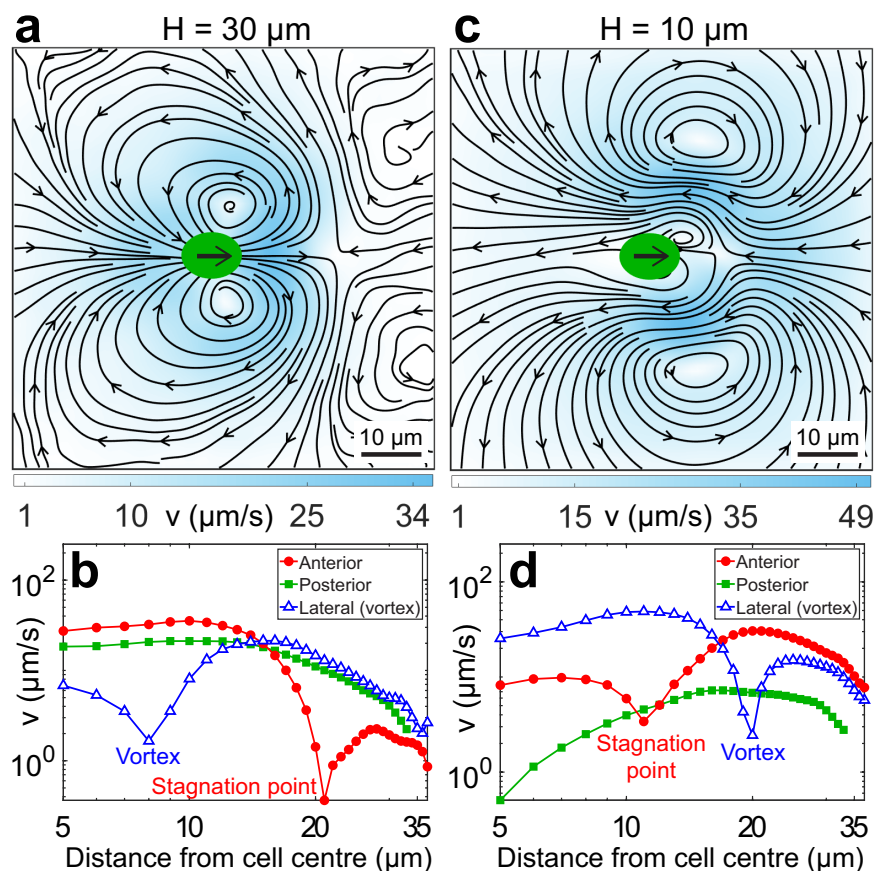


FIG. 3. **Experimental flow fields of Synchronous cells in weak and strong confinement.**

Experimentally measured, beat-averaged flow fields in the  $x - y$  plane of synchronously beating *Chlamydomonas* cells swimming in (a)  $H = 30 \mu\text{m}$ , (c)  $H = 10 \mu\text{m}$ . Black arrows on the cell body indicate that the cells are swimming to the right. Solid black lines indicate the streamlines of the flow in lab frame. The colorbars represent flow magnitude,  $v$ . The speed variation in (a), (c) along anterior, posterior and lateral to the cell (where the vortices are present) are respectively shown in (b) and (d).

not during cell body rotation about their swimming axis (Supplementary Movie S3), for appropriate comparison with planar H10 Synchronous swimmers. Figure 3a shows the velocity field for H30 cells obtained by averaging  $\sim 178$  beat cycles from 32 individual cells. It shows standard features of the CR's bulk flow field [38, 47] namely, far-field 4-loop flow of a puller, two lateral vortices at 8-9  $\mu\text{m}$  from cell centre and anterior flow along the swimming direction till a stagnation point, 21  $\mu\text{m}$  from the cell centre (Fig. 3b). These near-field flow characteristics are quite well explained theoretically by a 3-Stokeslet model [38] or a 3-bead model [48], where the thrust is distributed at approximate flagellar positions between two Stokeslets of strength  $(-1/2, -1/2)$  balanced by a  $+1$  Stokeslet due to viscous drag on the cell body.

The flow field of a representative H10 Synchronous swimmer ( $u = 5.67 \pm 1.57 \mu\text{m/s}$ ,  $\nu_b \sim 40 \text{ Hz}$ ) is shown in Fig. 3c, averaged over  $\sim 328$  beat cycles. The major striking difference between this strongly confined flow with that of the bulk is that the vortices contributing dominantly to the flow are opposite in sign. This is surprising and in stark contrast to the theoretical prediction that the far-field flow of a confined microswimmer is that of 2D source dipole pointing along the swimming direction (Supplementary Fig. S1a) [34, 35, 49]. On the contrary, the far-field looks more like a source dipole pointing opposite to the swimmer's motion. Other significant differences from the bulk flow include front-back flow asymmetry, opposite flow direction posterior to the cell, distant lateral vortices (20  $\mu\text{m}$ ) and closer stagnation point (11  $\mu\text{m}$ ) (Fig. 3d). All other H10 Synchronous swimmers, including the slowest ( $u \sim 0.15 \mu\text{m/s}$ ) and the fastest ( $u \sim 14 \mu\text{m/s}$ ) cells, show similar flow features.

A close examination suggests that the vortex contents of the flow fields of Figs. 3a (H30) and 3c (H10) are mutually compatible. The large vortices flanking the rapidly moving CR in H30 are shrunken and localized close to the cell body in H10 thanks to the greatly reduced swimming speed. The frontal vortices generated by flagellar motion now fills most of the visual field in H10. Generated largely during the power stroke of flagella, they are opposite in sense to the vortices produced by the moving cell body.

### Theoretical model of confined flow

In an attempt to explain the strongly confined CR's flow field, we begin by using the well-established far-field solution of a parallel Stokeslet between two plates by Liron & Mochon

[36]. However, the theoretical flow of Liron & Mochon decays much more rapidly than the experimental one and does not capture the vortex positions and flow variation of the experiment (Supplementary Note A and Fig. S1b-e).

We therefore start afresh from the incompressible 3D Stokes equation,  $-\nabla p(\mathbf{r}) + \eta \nabla^2 \mathbf{v}(\mathbf{r}) =$

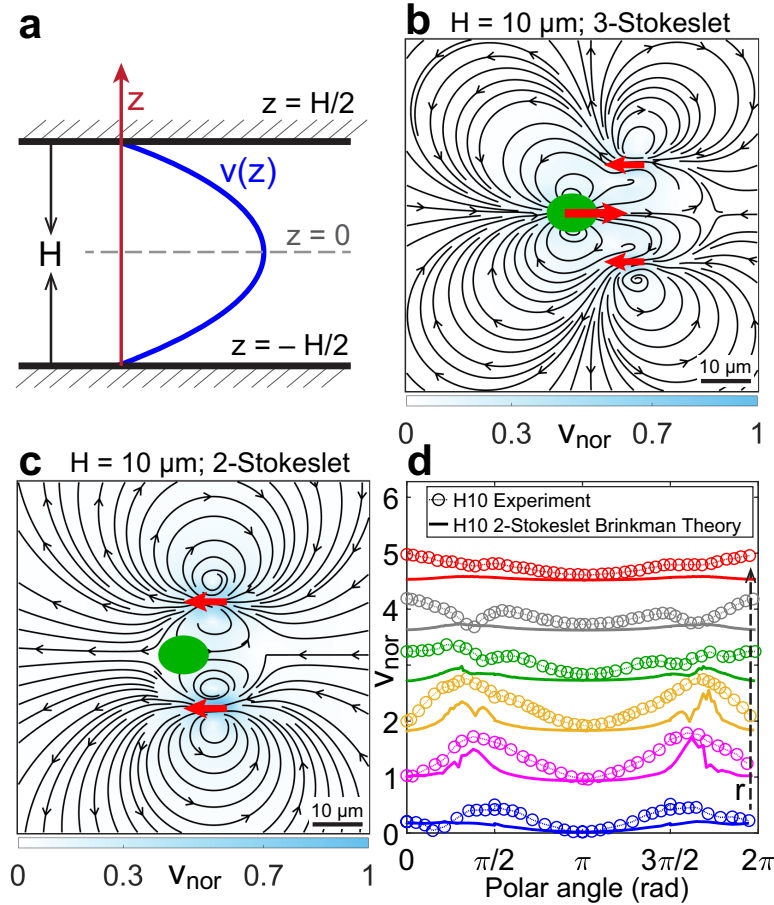


FIG. 4. **Theoretical model for flow field in strong confinement due to point sources.** (a) Schematic of flow profile along  $z$ -direction,  $v(z) \sim \cos(\pi z/H)$ , in a chamber of height  $H$  bounded by two solid walls. Theoretically computed flow fields for (b) 3-Stokeslet model and (c) 2-Stokeslet model using the quasi-2D Brinkman equation for  $H = 10 \mu\text{m}$  at the  $z = 0$  plane. The red arrows at (a)  $(0, 0)$ ,  $(12, \pm 10) \mu\text{m}$  and (b)  $(6, \pm 11) \mu\text{m}$  denote the position of the Stokeslets. The colorbars represent flow magnitudes normalised by their maximum,  $v_{nor}$ . (d) Comparison between normalised experimental (Fig. 3c) and theoretical flow field (4c) of a cell swimming in  $H = 10 \mu\text{m}$  along representative radial distances,  $r$  from the cell centre as a function of polar angle. From bottom to top,  $r = 6, 10, 14, 18, 22, 26 \mu\text{m}$ . Plots for each  $r$  denote the flow magnitudes for those grid points which lie in the radial gap  $(r, r + 1) \mu\text{m}$ . They are shifted along  $y$ -axis for clarity.

0,  $\nabla \cdot \mathbf{v}(\mathbf{r}) = 0$ , where  $p$  is the pressure field,  $\mathbf{v}$  and  $\eta$  are the fluid velocity and viscosity respectively. Next, we formulate an effective 2D Stokes equation and find its point force solution. In a quasi-2D chamber of height  $H$ , we consider an effective CR swimming in the  $z = 0$  plane of the coordinate system and the solid walls at  $z = \pm H/2$  (Fig. 4a). We consider the first Fourier mode for the velocity profile along  $z$  which satisfies the no-slip boundary condition  $\mathbf{v}(x, y, z = \pm H/2) = 0$  i.e.  $\mathbf{v}(x, y, z) = \mathbf{v}_0(x, y) \cos(\pi z/H)$ , where  $\mathbf{v}_0$  is the flow profile in the swimmer's  $x - y$  plane (Fig. 4a). Substituting this form of velocity field in the Stokes equation we obtain its quasi-2D Brinkman approximation [37] which, for a point force of strength  $\mathbf{F}$  at the  $z = 0$  plane, is

$$-\nabla_{xy} p(\mathbf{r}) + \eta \left( \nabla_{xy}^2 - \frac{\pi^2}{H^2} \right) \mathbf{v}(\mathbf{r}) + \mathbf{F} \delta(\mathbf{r}) = 0, \quad \nabla_{xy} \cdot \mathbf{v}(\mathbf{r}) = 0 \quad (1)$$

where  $p$  and  $\mathbf{v} \equiv \mathbf{v}_0$  are the pressure and fluid velocity in the  $x - y$  plane and  $\nabla_{xy} = \partial_x \hat{\mathbf{x}} + \partial_y \hat{\mathbf{y}}$ . We Fourier transform the above equation in 2D and invoke the orthogonal projection operator  $\mathbf{O}(\mathbf{k}) = 1 - \hat{\mathbf{k}}\hat{\mathbf{k}}$  to annihilate the pressure term and obtain the quasi-2D Brinkman equation in Fourier space

$$\mathbf{v}(\mathbf{k}) = \frac{\mathbf{O}(\mathbf{k}) \cdot \mathbf{F}}{\eta \left( k^2 + \frac{\pi^2}{H^2} \right)} \quad (2)$$

We inverse Fourier transform this equation in 2D for a Stokeslet oriented along the  $x$ -direction,  $\mathbf{F} = F \hat{\mathbf{x}}$  to obtain the flow field  $\mathbf{v}(\mathbf{r})$  at the  $z = 0$  plane (Supplementary Note B). This solution is superposed for one point source of strength +1 at cell centre  $(0, 0)$  and two point sources of strength  $-1/2$  each at approximate flagellar positions  $(x_f, \pm y_f) = (12, \pm 10) \mu\text{m}$ , all pointing along +ve  $x$  direction, which is the effective 3-Stokeslet model in 2D. The resulting solution has a 4-loop recirculating flow pattern and vorticity similar to that of bulk, but closer to the cell (Fig. 4b) [34]. This is in contrast to the experimental flow field of a H10 Synchronous swimmer which has only 2 dominant recirculating loops (Fig. 3c). Therefore, the 2D 3-Stokeslet model is an inappropriate description of the strongly confined flow. A closer look at the video microscopy of the H10 Synchronous swimmer (Supplementary Movie S1) shows that the cell is nearly stationary compared to the motion of its flagella. This can also be inferred from the ratio of the time taken by the cell body and flagellum to move by their respective body diameters,  $\tau_c/\tau_f$ , which is  $\sim 3200$  for strong confinement (H10) and  $\sim 178$  for weak confinement (H30). Therefore, the effect of cell drag is negligible when a CR is strongly confined. We verify our experimental insight, by

superposing only two flagellar Stokeslets and observe qualitatively similar streamlines and vortex flows with that of the experimental flow field (Fig. 4c). We note that the force density associated with a microswimmer in confinement will not in general integrate to zero as the solid boundaries act as momentum sinks [35, 50]. Therefore, another force is not required to balance the two flagellar Stokeslets in strong confinement. However, this theoretical ‘2-Stokeslet Brinkman flow’ (Fig. 4c) also decays faster than the experiment as shown in the radial comparison of these two flows in Fig. 4d. The root mean square deviation (RMSD, see Methods for definition) between these two flows is 24%.

With the experimental streamlines and vortices well described by a 2-Stokeslet Brinkman model, we now explain the slower flow variation in experiment. Strongly confined experi-

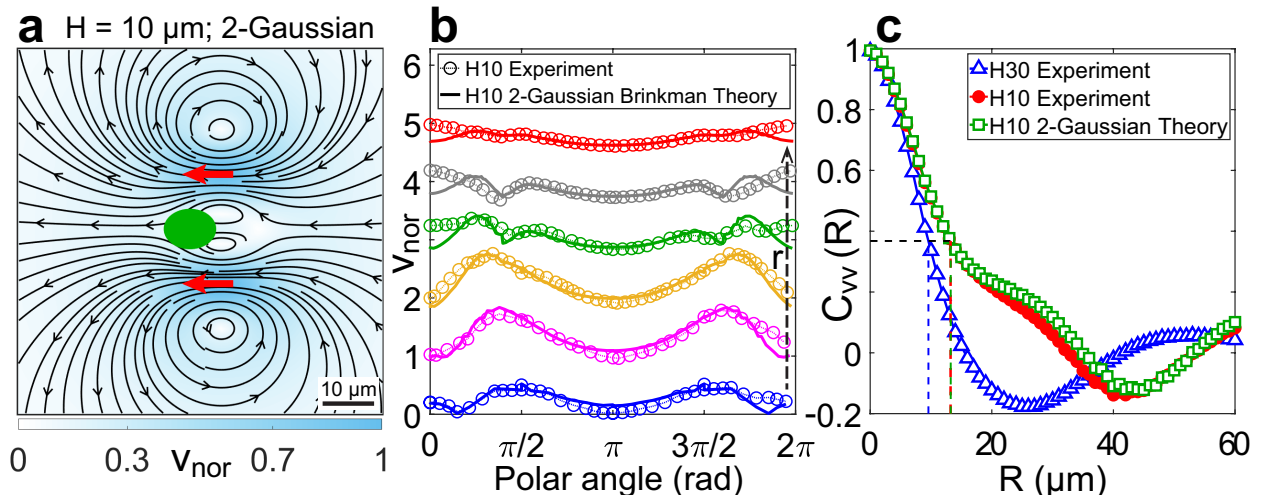


FIG. 5. **Theoretical flow field in strong confinement due to Gaussian sources.** (a) Theoretically computed flow field from 2-Gaussian sources at  $(6, \pm 11) \mu\text{m}$  (red arrows) using the quasi-2D Brinkman equation for  $H = 10 \mu\text{m}$  at the  $z = 0$  plane. The colorbar represents flow magnitude normalised by its maximum,  $v_{nor}$ . (b) Comparison between normalised experimental (Fig. 3c) and theoretical flow field (5a) of a cell swimming in  $H = 10 \mu\text{m}$  along representative radial distances,  $r$  from the cell centre as a function of polar angle. From bottom to top,  $r = 6, 10, 14, 18, 22, 26 \mu\text{m}$ . Plots for each  $r$  denote the flow magnitudes for those grid points which lie in the radial gap  $(r, r + 1) \mu\text{m}$ . They are shifted along  $y$ -axis for clarity. (c) Normalised radial velocity-velocity correlation function,  $C_{vv}(R)$ , of flow fields in Fig. 3a,c and 5a. The dashed vertical lines denote the characteristic length scales,  $\lambda$ , for flows where the correlation function decays to  $1/e$  (horizontal dashed line).  $\lambda = 9.6 \mu\text{m}$  for  $H = 30 \mu\text{m}$  and  $\lambda = 13.2 \mu\text{m}$  for  $H = 10 \mu\text{m}$ , both experiment and theory.

mentally observed flow is mostly ascribed to the flagellar thrust due to distinct time scales of cellular and flagellar motion, as discussed above. Clearly, a delta-function point source will not be adequate to describe flagellar propulsive thrust as they are slender rods of length  $L \sim 11 \mu\text{m}$ . We, therefore, associate a 2D Gaussian source  $g(\mathbf{r}) = \frac{e^{-r^2/2\sigma^2}}{2\pi\sigma^2}$  of standard deviation  $\sigma$ , to Eq. (1) instead of the point-source  $\delta(\mathbf{r})$ . Thus the quasi-2D Brinkman equation in Fourier space (2) for a Gaussian source gets modified to

$$\mathbf{v}(\mathbf{k}) = \frac{\mathbf{O}(\mathbf{k}) \cdot \mathbf{F}}{\eta \left( k^2 + \frac{\pi^2}{H^2} \right)} e^{-k^2\sigma^2/2} . \quad (3)$$

Superposing the inverse Fourier transform of the above equation for two sources of  $\mathbf{F} = (-1/2, -1/2) \hat{\mathbf{x}}$  at  $(x_f, \pm y_f) = (6, \pm 11) \mu\text{m}$  with  $\sigma \sim L/2 = 5 \mu\text{m}$ , we obtain the theoretical flow shown in Fig. 5a, which has 8% RMSD with the experimental flow. Comparing these two flows along representative radial distances from the cell centre as a function of polar angle show a good agreement (Fig. 5b). Notably, Fig. 5a i.e. the ‘2-Gaussian Brinkman flow’ has captured the flow variation and most of the experimental flow features accurately. Specifically, these are the lateral vortices at  $20 \mu\text{m}$  and an anterior stagnation point at  $13 \mu\text{m}$  from cell centre. The only limitation of this theoretical model is that it cannot account for the front-back asymmetry of the strongly confined flow, as is evident from Fig. 5b for the polar angles  $0$  or  $2\pi$  and  $\pi$  which correspond to ahead of and behind the cell, respectively. This deviation is more pronounced in the frontal region as the cell body squished between the two solid walls mostly blocks the forward flow from reaching the cell posterior. Thus, the no-slip boundary on the cell body needs to be invoked to mimic the front-back flow asymmetry, which is a more involved analysis due to the presence of multiple boundaries and can be addressed in a follow-up study.

Now that we have explained the flow field of CR in strong confinement, we test our quasi-2D Brinkman theory in weak confinement,  $H = 30 \mu\text{m}$ . The cell speed is 30 times faster than that in strong confinement. Hence, we use the conventional 3-Stokeslet model for CR, but with a Gaussian distribution for each point source. We, therefore, superpose the solution of Eq. (3) for 3-Gaussian sources representing the cell body and two flagella in  $H = 30 \mu\text{m}$ . The resulting flow field (Supplementary Fig. S2) matches qualitatively with the experimental flow field of CR in weak confinement (Fig. 3a), with 14% RMSD. This deviation is expected in weak confinement,  $H \approx 3D$ , because the quasi-2D theoretical approximation is mostly valid at  $H \approx D$ .

We now calculate the normalised spatial velocity-velocity correlation function of these flows,  $C_{vv}(R) = \frac{\langle \mathbf{v}(r) \cdot \mathbf{v}(r+R) \rangle}{\langle \mathbf{v}(r) \cdot \mathbf{v}(r) \rangle}$  to estimate the enhancement in fluid mixing in strong confinement which is also evident in the videos of cell suspensions containing tracer particles (Supplementary Movie S1, Fig. 5c). The characteristic decay length scale of flows,  $\lambda$ , is 13.2  $\mu\text{m}$  for the strongly confined flow, which is 37.5% higher than the weakly confined flow in  $H = 30 \mu\text{m}$  ( $\lambda = 9.6 \mu\text{m}$ ), even though the cell is swimming very slowly in strong confinement.

## DISCUSSION

Confined microswimmers are of great ecological, biophysical and technological importance and an abundance of situations arises in which the flow field dominates the relevant response or effect [17, 19, 22, 27, 51]. For example, predator-prey, nutrient uptake, physiological development, cargo transport, micromixing, drug delivery and sensing all rely on setting up and regulating the fluid flows involved. Our results show that a prototypical active puller like CR under strong confinement has a strikingly different motility and flow field from that of a bulk swimmer, which leads to enhancement in fluid mixing. The decrease in cell speed with increasing confinement, which arises due to mechanical friction from the walls and not due to behavioural change, leads to an opposite lateral flow vorticity compared to that of the bulk. 2-Gaussian Brinkman flow describes these features more effectively compared to the conventional 3-Stokeslet model of CR. This theoretical approach can also be easily utilised to analyse flows of a dilute collection of strongly confined swimmers (Supplementary Note C and Fig. S3). Taken together, we show that the far-field flow of a puller type of force dipole swimmer not only reduces to a 2D source dipole under strong confinement, the direction of the source dipole becomes opposite to the cell's swimming direction, contrary to predictions from theories in which the fundamental force-density content is assumed to remain unchanged as confinement is tightened [34, 35]. These results are complementary to other theoretical and experimental studies on confined microswimmer flows where the effect of confinement on motility was either ignored [34, 35] or observed to be insignificant [49]. Our methodology is completely general and therefore can be used to test whether hard-wall confinement will similarly induce substantial changes in flows of active pushers and other kinds of microswimmers. We expect our work to inspire further studies to determine the enhancement of fluid mixing due to hard wall confinement of concentrated active suspensions

[52, 53]. These effects can be exploited in microfluidic devices for efficient control, navigation and trapping of microbes and synthetic swimmers [5, 27, 28, 54].

## METHODS

**Surface modification of microspheres and glass surfaces.** The CR culture medium of TAP+P contains divalent ions such as  $\text{Ca}^{2+}$ ,  $\text{Mg}^{2+}$ ,  $\text{SO}_4^{2-}$  which decrease the screening length of the 200 nm negatively charged microspheres, thereby promoting inter-particle aggregation and sticking to glass surfaces and CR’s flagella. Therefore, the sulfate microspheres (S37491, Thermo Scientific) are sterically stabilised by grafting long polymer chains of polyethylene glycol (mPEG-SVA-20k, NANOCS, USA) with the help of a positively charged poly-L-lysine backbone (P7890, 15-30kDa, Sigma) [55, 56]. In addition, the coverslip and slide surfaces are also cleaned and coated with polyacrylamide brush to prevent non-specific adhesion of microspheres and flagella to the glass surfaces, prior to sample injection [56].

**Sample imaging.** The sample chamber containing CR and tracers is mounted on an inverted microscope (Olympus IX83/IX73) and placed under red light illumination ( $> 610$  nm) for 40 minutes to let the cells acclimatize, before recording any data. All flow field data, flagellar waveform and cellular trajectory (except for Fig. 2a) are captured using a 40X phase objective (Olympus, 0.65 NA, Plan N, Ph2) coupled to a high speed CMOS camera (Phantom Miro C110, Vision Research, pixel size =  $5.6 \mu\text{m}$ ) at 500 frames/s. As CR cells move faster in  $H = 30 \mu\text{m}$  chamber, a 8.2 second long trajectory cannot be captured at that magnification. So we used a 10X objective in bright field (Olympus, 0.25 NA, PlanC N) connected to a high speed camera of higher pixel length (pco.1200hs, pixel size =  $12 \mu\text{m}$ ) at 100 frames/s to capture 8.2 s long trajectories of cells in  $H = 30 \mu\text{m}$  chamber (Fig. 2a).

**Height measurement of sample chamber.** We use commercially available double tapes of thickness 10 and  $30 \mu\text{m}$  (Nitto Denko Corporation) as spacer between the glass slide and coverslip. To measure the actual separation between these two surfaces, we stick 200 nm microspheres to a small strip ( $18 \times 6 \text{ mm}^2$ ) on both the glass surfaces by heating a dilute solution of microspheres. Next, we inject immersion oil inside the sample chamber to prevent geometric distortion due to refractive index mismatch between objective immersion medium and sample. The chamber height is then measured by focusing the stuck microspheres on both surfaces through a 60X oil-immersion phase objective (Olympus, 1.25 NA). We find

the measured chamber height for the 10  $\mu\text{m}$  spacer to be  $10.88 \pm 0.68 \mu\text{m}$  and for the 30  $\mu\text{m}$  spacer to be  $30.32 \pm 0.87 \mu\text{m}$ , from 8 different samples in each case.

**Particle Tracking Velocimetry (PTV).** In phase contrast microscopy, the edge of CR’s cell body appear as a dark line (Fig. 1a,b,c), which is detected using the Ridge Detection plugin in ImageJ [57, 58]. An ellipse is fitted to the pixelated CR’s edge and the major axis vertex in between the two flagellum is identified through custom-written Matlab codes. The cell body is masked and the tracers’ displacement in between two frames (time gap, 2 ms) are calculated in the lab frame using standard Matlab tracking routines [59]. The velocity vectors obtained from multiple beat cycles are translated and rotated to the a common coordinate system where the cell’s major axis is pointing to the right (Fig. 3a,c). Outliers with velocity magnitude more than six standard deviations from the mean are deleted. The resulting velocity vectors from all beat cycles (including those from different cells in  $H = 30 \mu\text{m}$ ) are then placed on a mesh grid of size  $2.24 \times 2.24 \mu\text{m}^2$  and the mean at each grid point is computed. The gridded velocity vectors are then smoothened using a  $5 \times 5$  averaging filter. Furthermore, for comparison with theoretical flow, the  $x$  and  $y$  components of the velocity vectors are interpolated on a gridsize of  $1 \times 1 \mu\text{m}^2$ . Streamlines are plotted using the ‘*streamslice*’ function in Matlab.

**Trajectory tortuosity.** Tortuosity characterizes the number of twists or loops in a cell’s trajectory. It is given by the ratio of arclength to end-to-end distance between two points in a trajectory. We divide each trajectory into segments of arc-length  $\approx 20 \mu\text{m}$ . We calculate the tortuosity for individual segments and find their mean for each trajectory. We consider the trajectories of all cells whose mean speed  $> 1 \mu\text{m/s}$  and are imaged at 500 frames/s through 40X objective. There were 52 H30 cells, 35 H10 Wobblers and 23 H10 Synchronous cells which satisfied these conditions and the data from these cells constitute Fig. 2g.

**Root Mean Square Deviation (RMSD).** The match between experimental and theoretical flow fields is quantified by root mean square deviation (RMSD) of their velocity magnitudes.  $RMSD = \sqrt{\sum_{j=1}^{NG} (v_j^{expt} - v_j^{th})^2 / NG}$ , where  $v_j^{expt}$  and  $v_j^{th}$  are the experimental and theoretical magnitudes of the velocity fields at the  $j$ -th grid point, respectively and  $NG$  is the total number of grid points.

**Acknowledgements:** This work is supported by the Wellcome Trust/DBT India Alliance Fellowship [grant number IA/I/16/1/502356] awarded to P.S. S.R. acknowledges support from a J C Bose Fellowship of the SERB (India) and the Tata Education and Develop-

ment Trust. D.M. and P.S. acknowledge Ayantika Khanra, Aparna Baskaran and Ronojoy Adhikari for useful discussions.

**Author Contributions:** D.M. and P.S. conceived and designed the experiments. D.M. performed the experiments. S.R. proposed the theoretical model. A.G.P. and D.M. performed the calculations. D.M., P.S. and S.R. interpreted the experiments and wrote the manuscript.

**Competing financial interests:** The authors declare no competing financial interests.

**Data availability:** The data that support the findings of this study are available from the corresponding author on request.

- 
- [1] J. Elgeti, R. G. Winkler, and G. Gompper, [Reports on Progress in Physics](#) **78**, 056601 (2015).
  - [2] A. Ghosh and P. Fischer, [Nano letters](#) **9**, 2243 (2009).
  - [3] W. Duan, W. Wang, S. Das, V. Yadav, T. E. Mallouk, and A. Sen, [Annual Review of Analytical Chemistry](#) **8**, 311 (2015).
  - [4] R. Dreyfus, J. Baudry, M. L. Roper, M. Fermigier, H. A. Stone, and J. Bibette, [Nature](#) **437**, 862 (2005).
  - [5] A. Barbot, D. Decanini, and G. Hwang, [Scientific Reports](#) **6**, 19041 (2016).
  - [6] S. Ramaswamy, [Annual Review of Condensed Matter Physics](#) **1**, 323 (2010).
  - [7] H. H. Wensink, J. Dunkel, S. Heidenreich, K. Drescher, R. E. Goldstein, H. Löwen, and J. M. Yeomans, [Proceedings of the National Academy of Sciences](#) **109**, 14308 (2012).
  - [8] H. C. Berg, [Proceedings of the National Academy of Sciences](#) **93**, 14225 (1996).
  - [9] I. H. Riedel, K. Kruse, and J. Howard, [Science](#) **309**, 300 (2005).
  - [10] M. M. Genkin, A. Sokolov, O. D. Lavrentovich, and I. S. Aranson, [Phys. Rev. X](#) **7**, 011029 (2017).
  - [11] C. Krüger, G. Klös, C. Bahr, and C. C. Maass, [Phys. Rev. Lett.](#) **117**, 048003 (2016).
  - [12] E. M. Purcell, [American Journal of Physics](#) **45**, 3 (1977).
  - [13] E. Lauga and T. R. Powers, [Reports on Progress in Physics](#) **72**, 096601 (2009).
  - [14] M. C. Marchetti, J. F. Joanny, S. Ramaswamy, T. B. Liverpool, J. Prost, M. Rao, and R. A. Simha, [Rev. Mod. Phys.](#) **85**, 1143 (2013).
  - [15] D. Saintillan, [Annual Review of Fluid Mechanics](#) **50**, 563 (2018).
  - [16] T. J. Pedley and J. O. Kessler, [Annual Review of Fluid Mechanics](#) **24**, 313 (1992).

- [17] J. C. Conrad and R. Poling-Skutvik, [Annual Review of Chemical and Biomolecular Engineering](#) **9**, 175 (2018).
- [18] L. Hall-Stoodley, J. W. Costerton, and P. Stoodley, [Nature Reviews Microbiology](#) **2**, 95 (2004).
- [19] P. Denissenko, V. Kantsler, D. J. Smith, and J. Kirkman-Brown, [Proceedings of the National Academy of Sciences](#) **109**, 8007 (2012).
- [20] V. Kantsler, J. Dunkel, M. Polin, and R. E. Goldstein, [Proceedings of the National Academy of Sciences](#) **110**, 1187 (2013).
- [21] A. P. Berke, L. Turner, H. C. Berg, and E. Lauga, [Phys. Rev. Lett.](#) **101**, 038102 (2008).
- [22] W. Foissner, [European Journal of Protistology](#) **34**, 195 (1998).
- [23] E. Lauga, [Annual Review of Fluid Mechanics](#) **48**, 105 (2016).
- [24] E. Lushi, H. Wioland, and R. E. Goldstein, [Proceedings of the National Academy of Sciences](#) **111**, 9733 (2014).
- [25] A. C. H. Tsang and E. Kanso, [Phys. Rev. Lett.](#) **116**, 048101 (2016).
- [26] Rothschild, [Nature](#) **198**, 1221 (1963).
- [27] A. Karimi, S. Yazdi, and A. M. Ardekani, [Biomicrofluidics](#) **7**, 21501 (2013).
- [28] B.-W. Park, J. Zhuang, O. Yasa, and M. Sitti, [ACS Nano](#) **11**, 8910 (2017).
- [29] R. E. Goldstein, [Annual Review of Fluid Mechanics](#) **47**, 343 (2015).
- [30] S. Rafai, L. Jibuti, and P. Peyla, [Phys. Rev. Lett.](#) **104**, 098102 (2010).
- [31] S. Sasso, H. Stibor, M. Mittag, and A. R. Grossman, [eLife](#) **7**, e39233 (2018).
- [32] P. M. Schenk, S. R. Thomas-Hall, E. Stephens, U. C. Marx, J. H. Mussnug, C. Posten, O. Kruse, and B. Hankamer, [BioEnergy Research](#) **1**, 20 (2008).
- [33] M. Siaux, S. Cuiné, C. Cagnon, B. Fessler, M. Nguyen, P. Carrier, A. Beyly, F. Beisson, C. Triantaphylidès, Y. Li-Beisson, and G. Peltier, [BMC Biotechnology](#) **11**, 7 (2011).
- [34] A. J. T. M. Mathijssen, A. Doostmohammadi, J. M. Yeomans, and T. N. Shendruk, [Journal of Fluid Mechanics](#) **806**, 3570 (2016).
- [35] T. Brotto, J.-B. Caussin, E. Lauga, and D. Bartolo, [Phys. Rev. Lett.](#) **110**, 038101 (2013).
- [36] N. Liron and S. Mochon, [Journal of Engineering Mathematics](#) **10**, 287 (1976).
- [37] H. C. Brinkman, [Flow, Turbulence and Combustion](#) **1**, 27 (1949).
- [38] K. Drescher, R. E. Goldstein, N. Michel, M. Polin, and I. Tuval, [Phys. Rev. Lett.](#) **105**, 168101 (2010).
- [39] J. Alper, V. Geyer, V. Mukundan, and J. Howard, in [Methods in enzymology](#), Vol. 524

- (Elsevier, 2013) pp. 343–369.
- [40] O. A. Sineshchekov, K.-H. Jung, and J. L. Spudich, [Proceedings of the National Academy of Sciences](#) **99**, 8689 (2002).
  - [41] C. T. Kreis, M. Le Blay, C. Linne, M. M. Makowski, and O. Bäümchen, [Nature Physics](#) **14**, 45 (2018).
  - [42] M. Polin, I. Tuval, K. Drescher, J. P. Gollub, and R. E. Goldstein, [Science](#) **325**, 487 (2009).
  - [43] H. Kurtuldu, D. Tam, A. E. Hosoi, K. A. Johnson, and J. P. Gollub, [Phys. Rev. E](#) **88**, 013015 (2013).
  - [44] A. Qin, B. and Gopinath, J. Yang, J. P. Gollub, and P. E. Arratia, [Scientific Reports](#) **5**, 9190 (2015).
  - [45] K. W. Foster and R. D. Smyth, [Microbiological reviews](#) **44**, 572 (1980).
  - [46] S. K. Choudhary, A. Baskaran, and P. Sharma, [Biophysical Journal](#) **117**, 1508 (2019).
  - [47] J. S. Guasto, K. A. Johnson, and J. P. Gollub, [Phys. Rev. Lett.](#) **105**, 168102 (2010).
  - [48] L. Jibuti, W. Zimmermann, S. Rafai, and P. Peyla, [Phys. Rev. E](#) **96**, 052610 (2017).
  - [49] R. Jeanneret, D. O. Pushkin, and M. Polin, [Phys. Rev. Lett.](#) **123**, 248102 (2019).
  - [50] A. Maitra, P. Srivastava, M. C. Marchetti, S. Ramaswamy, and M. Lenz, [Phys. Rev. Lett.](#) **124**, 028002 (2020).
  - [51] M. Fletcher and K. C. Marshall, “Are solid surfaces of ecological significance to aquatic bacteria?” in [Advances in Microbial Ecology: Volume 6](#), edited by K. C. Marshall (Springer US, Boston, MA, 1982) pp. 199–236.
  - [52] H. Kurtuldu, J. S. Guasto, K. A. Johnson, and J. P. Gollub, [Proceedings of the National Academy of Sciences](#) **108**, 10391 (2011).
  - [53] D. O. Pushkin and J. M. Yeomans, [Journal of Statistical Mechanics: Theory and Experiment](#) **2014**, P04030 (2014).
  - [54] M. J. Kim and K. S. Breuer, [Analytical Chemistry](#) **79**, 955 (2007).
  - [55] T. Sanchez, D. T. Chen, S. J. DeCamp, M. Heymann, and Z. Dogic, [Nature](#) **491**, 431 (2012).
  - [56] D. Mondal, R. Adhikari, and P. Sharma, Preprint at [arXiv:1904.07783](#) (2019), [arXiv:1904.07783](#).
  - [57] C. Steger, [IEEE Transactions on Pattern Analysis and Machine Intelligence](#) **20**, 113 (1998).
  - [58] T. Wagner and M. Hiner, [Detect ridges/lines with ImageJ: Ridge Detection 1.4.0](#) (2017).
  - [59] D. Blair and E. Dufresne, [Particle-tracking code available at http://physics.georgetown.edu/matlab](#) (2008).